ORIGINAL PAPER

High-pressure phase relations in the system Fe–Ni–Cu–S up to 14 GPa: implications for the stability of sulfides in the earth's upper mantle

Christopher Beyer[1] · Thilo Bissbort[1,2] · Rebecca Hartmann[1] · Jasper Berndt[3] · Stephan Klemme[3] · Raúl O. C. Fonseca[1]

Abstract

Base metal sulfides (Fe–Ni–Cu–S) are ubiquitous phases in mantle and subduction-related lithologies. Sulfides in the mantle often melt incongruently, which leads to the production of a Cu–Ni-rich sulfide melt and leaves a solid residue called mono-sulfide solid solution (mss). However, the persistence of crystalline sulfide phases like mss in the Earth's mantle at higher temperatures and pressures deep within the Earth has long been up for debate, as the presence of both mss and sulfide melt in mantle rocks implies the fractionation of chalcophile elements during mantle melting. Recent studies have shown that the average mantle sulfide (45 wt.% Fe, 16 wt.% Ni, 1 wt.% Cu, and 38 wt.% S), is fully molten at average mantle potential temperatures (1300–1400 °C) up to 8 GPa (ca. 240 km). However, sulfide inclusions found in diamonds show a broad compositional spectrum, ranging from Ni-poor and Fe-rich (eclogitic), to Ni-rich and Fe-poor sulfides (peridotitic), with their Cu contents being generally low. The wide compositional variety of diamond-hosted sulfide inclusions raises the possibility that results on the melting properties obtained from this average mantle sulfide compositional may not reflect that found in those inclusions. As such, further investigation of the melting properties of sulfides from a wide compositional range is necessary. Here, we present the results of an experimental study where the melting properties of typical sulfide compositions found in diamond inclusions associated with eclogites and peridotites have been determined. Experiments have been carried out between 0.1 MPa and 14 GPa, and between 920 and 1590 °C, on box muffle furnaces, end-loaded piston cylinder, and multi-anvil apparatuses. Results show that solid mss in Fe-rich, Ni-poor sulfide inclusions associated with eclogites persist to higher pressures and temperatures compared to their less-refractory, more Ni-rich peridotitic counterparts to the depth of the mantle transition zone (410 km depth). Our results have implications for the recycling of chalcophile elements during subduction-related processes and the entrapment of sulfides in diamonds.

Keywords Sulfides · Phases · Siderophile elements · Melting relationships

Introduction

Base metal sulfides (BMS – Fe–Ni–Cu–S +/- Co and Zn) are ubiquitous accessory phases in basalts, peridotites, and mantle xenoliths (Dromgoole and Pasteris 1987), and are the most frequent inclusions found in diamonds (Chaussidon et al. 1987; Pearson et al. 1998; Stachel and Harris 2008). Effectively, all the sulfur found in Earth's mantle resides in discrete sulfides. This behavior contrasts with that of H_2O, which can substitute into the common mantle silicates (e.g., olivine and pyroxenes—cf. (Padrón-Navarta and Hermann 2017; Férot and Bolfan-Casanova 2012; Bolfan-Casanova et al. 2000), among others) and thus behaves like a trace element during mantle melting (e.g., Bolfan-Casanova et al. (2000)). Sulfur, on the other hand, does not. Of all trace elements in the mantle, only carbon is so incompatible in silicates that it must form its own phase at typical mantle abundances (see review by Stagno (2019)). Due to their nature, sulfides are a sink for highly siderophile elements (HSE), as well as economically important chalcophile elements like Cu, Zn, Ag, and Pb. Sulfides strongly

✉ Christopher Beyer
  christopher.c.beyer@rub.de

1 Institut für Geologie, Mineralogie und Geophysik, Ruhr-Universität Bochum, 44801 Bochum, Germany

2 Central Unit for Ionbeams and Radionuclides (RUBION), Ruhr-Universität Bochum, 44801 Bochum, Germany

3 Institut für Mineralogie, Westfälische Wilhelms-Universität Münster, 48149 Münster, Germany

affect chalcophile element behavior in a range of geological contexts and pressure and temperature conditions that are relevant to planetary formation and differentiation, making their study of paramount importance.

Over the last two decades, sulfide inclusions found in diamonds have been widely used to track the life cycle of diamonds and to gain insight into how they form (Pearson et al. 1998; Westerlund et al. 2006; Aulbach et al. 2009). Because diamonds are inert to most of their inclusions and are stable over a wide range of pressures and temperatures prevalent in Earth's interior, inclusions in diamonds are perfectly suited to track the evolution of Earth's mantle. Diamond-hosted sulfide inclusions thus offer a window into sulfide formation and cycling in the deep Earth, as they are more likely to record the conditions of sulfide formation in Earth's mantle when compared to sulfides found in mantle xenoliths, which are prone to metasomatic and thermal overprint (cf. Harvey et al. 2010).

Magmatic and metamorphic sulfides display a rich mineralogical diversity, with the most important sulfide minerals comprising the high-temperature monosulfide solid solution (mss) and intermediate solid solution (iss), which break down to the lower temperature pyrrhotite, pentlandite, and chalcopyrite upon cooling (see review by Eggler and Lorand 1993). These phases have distinct physical and chemical properties that determine their stability in P-T-fO_2 -fS_2 space, and thus determine the sulfur buffer capacity and partitioning of siderophile and chalcophile elements of their host rock. The effect of pressure, temperature, fO_2, and fS_2 on sulfide stability and their formation in Earth's mantle is not yet constrained for compositions other than mss, and only up to pressures and temperatures as high as 8 GPa and 1450 °C, respectively (Tsuno and Dasgupta 2015; Zhang and Hirschmann 2016) (Fig. 1). Surprisingly, the range of sulfide compositions that have been studied experimentally covers only a narrow compositional domain (Bockrath et al. 2004; Ballhaus et al. 2006; Zhang and Hirschmann 2016). As such, most experimental studies have been restricted to investigating either the simple Fe–S–O system or the more complex Cu–Fe–Ni–S-(±O) system. Moreover, the narrow range of Ni concentrations in the bulk sulfides (15–20 wt.%) used in these studies is set by the equilibrium with upper mantle olivine (Fo90) with 3000 µg/g Ni (Eggler and Lorand 1993; Bockrath et al. 2004; Zhang and Hirschmann 2016). However, natural diamond- and olivine-hosted sulfide inclusions cover a much wider compositional space in the Fe–Ni–S ternary. For example, the amount of Ni in these sulfide inclusions varies between 5 and ~45 at.% (cf. Fig. 1 of Zhang and Hirschmann 2016). One reason for this reported variability is the paragenesis of the natural inclusions. Peridotitic inclusions are generally richer in Ni, whereas their eclogitic counterparts usually contain less than 12 wt.% Ni, based on a set of 40 inclusions from Yakutian diamonds (Bulanova
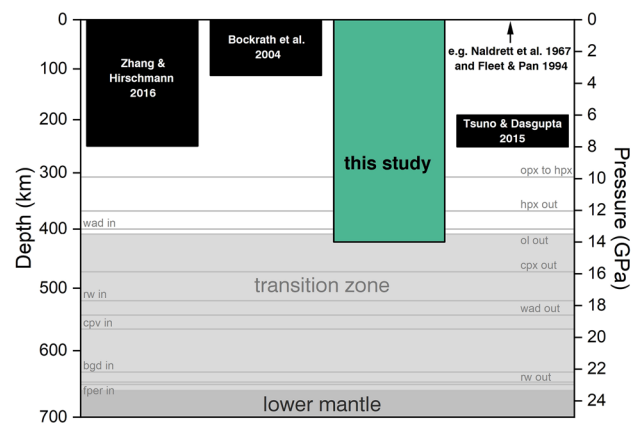

Fig. 1 Range of high-pressure and high-temperature experiments conducted in the system Fe–Ni–Cu–S (Naldrett et al. 1967; Fleet and Pan 1994; Bockrath et al. 2004; Tsuno and Dasgupta 2015; Zhang and Hirschmann 2016). Phase transitions are based on a model pyrolite (Stixrude and Lithgow 2005) calculated along a mantle geotherm (Anderson 1982). *opx* orthopyroxene, *hpx* high-pressure clinoenstatite, *wad* wadsleyite, *ol* olivine, *cpx* clinopyroxene, *rw* ringwoodite, *cpv* Ca-perovksite, *brd* bridgmanite, *fper* ferropericlase

et al. 1996) (Fig. 2). Intriguingly, some inclusions in diamonds that may have formed in the uppermost lower mantle contain low-Ni sulfides (e.g., pyrrhotite) with Ni concentrations between 0.3 and 3 wt.%, which has been interpreted to represent an eclogitic origin for these diamonds (Bulanova et al. 2010).

Shirey et al. (2019) emphasized that Fe–Ni–Cu–S inclusions are more abundant than expected relative to silicate inclusions in diamonds, and proposed that a genetic link between sulfides and diamonds must exist. Hence, an experimental investigation at conditions that overlap with the stability field of lithospheric and sub-lithospheric diamonds (4–16 GPa and 1000–1600° C) is long overdue. Sub-lithospheric diamonds, in particular, might play a key role in understanding the cycling of volatile elements (e.g., species of C, O, H, N, and S) in the mantle transition zone and the uppermost lower mantle (Pearson et al. 2014; Thomson et al. 2014; Beyer and Frost 2017; Shirey et al. 2019). This underlines the need to complement existing studies, conducted at conditions representative of the lithospheric mantle, with experiments carried out at sub-lithospheric mantle conditions (i.e., below 200 km depths to the base of the upper mantle).

In this contribution, the nature of mantle sulfides, and their phase relationships, have been investigated at variable pressure (0.1 MPa to 14 GPa) and temperature (850–1590 °C) over a range of bulk compositions typically found in inclusions hosted by peridotitic and eclogitic mantle xenoliths. We show that the persistence of liquidus crystalline sulfides along natural mantle geotherms is highly dependent on their Ni content and that sulfides of eclogitic affinity are
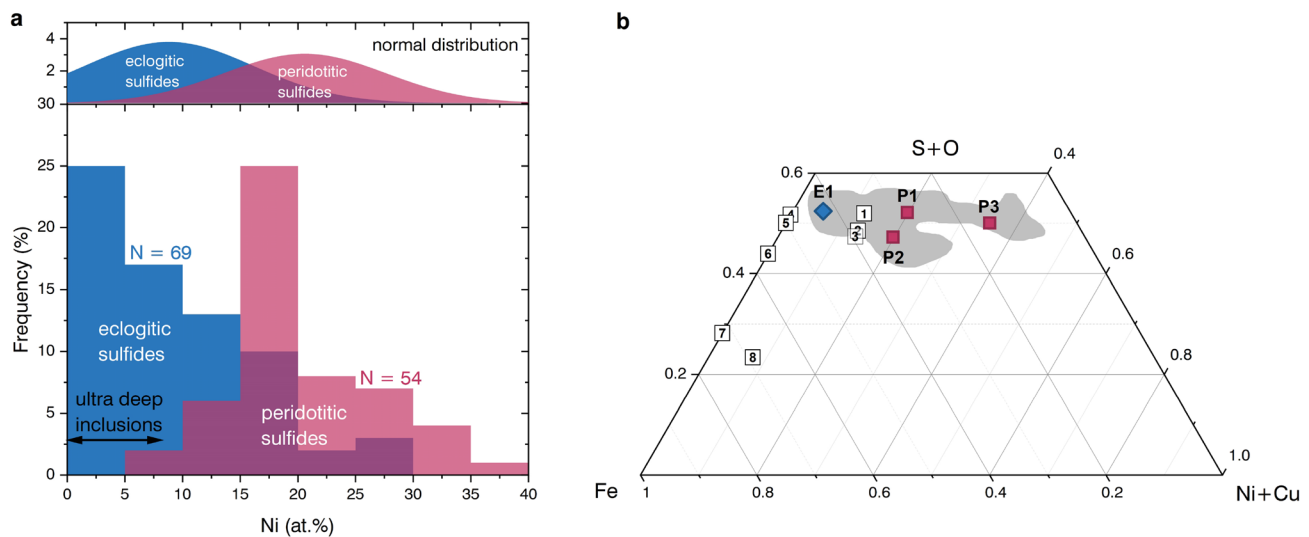
Fig. 2 **a** Histogram of sulfide inclusions found in eclogitic and peridotitic diamonds (based on the data of Bulanova et al. (1996); Westerlund et al. (2006); Aulbach et al. (2009), grey field). **b** Ternary diagram with O projected on S and Cu projected on Ni. Starting compositions in this study are eclogitic E1 and peridotitic P1, P2, and P3 sulfides, and are reported in Table 1. They were selected to probe the compositional range of natural sulfide inclusions that are found in diamonds (grey field). Numbers refer to compositions that were used in previous studies, with Zhang and Hirschmann (2016) = 1, Bockrath et al. (2004) = 1, Sharp (1969) = 4, Boehler (1992) = 5, Boehler (1996) = 6, Ballhaus et al. (2006) = 2, 3, Ryzhenko and Kennedy (1973) = 4, 6, Urakawa et al. (1987) = 7, 8

overall more refractory than their peridotitic counterparts and thus more likely to persist as residual phases during melting at higher pressures and temperatures. These results have strong implications for chalcophile element cycling in subduction-related settings, and how these elements are recycled into Earth's mantle.

Experimental and analytical methods

Experimental methods

Bulk compositions were prepared by adding Fe, Ni, and Cu metal powders to elemental sulfur, following a similar procedure as outlined in Helmy et al. (2010) (Table 1). The mixes were then ground thoroughly in an agate mortar and placed inside 6 mm outer diameter SiO_2 glass tubes and welded shut with a hydrogen-oxygen torch while under a vacuum (ca. 1 Pa). Sample powders were subsequently pre-reacted by stepwise heating to 900 °C to form homogeneous sulfide phases. The pre-reacted sulfides were then reground until homogeneous and used for subsequent piston cylinder and multi-anvil experiments.

High-pressure experiments were carried out in a 630 t Walker-type multi-anvil apparatus located at the Ruhr-University Bochum. A 14/8 (14 mm octahedron edge length, 8 mm truncated edge length) octahedral pressure medium was used for experiments carried out at 8 GPa and a 10/4 octahedral pressure medium for experiments conducted at 14 GPa. The octahedron consists of Cr_2O_3-doped magnesium oxide (*Ceramic Substrates*, Isle of Wight), a zirconium oxide insulator (*OZ8C, Mino Ltd.*, Japan) and, depending on pressure, either a stepped graphite heater (up to 8 GPa) or a 50 μm thick rhenium-foil heater (14 GPa). The inner parts of the pressure medium were filled with crushable MgO (RM98TE, *Rauschert GmbH*) and ZrO_2 (10/4) plugs. A type-D thermocouple ($W_{97}Re_3$-$W_{75}Re_{25}$) was introduced axially using a quad-bore alumina tube surrounded by a crushable MgO sleeve. Cavities around the thermocouple tip were padded with alumina powder to protect the thermocouple during compression and prevent the deformation of the assembly around its tip. Both single-chamber and multi-chamber sample containers fabricated from crushable MgO and SiO_2 glass have been used. The dimensions of the assemblies and capsules are shown in Fig. 3. Each experiment was slowly compressed to the target pressure (4–6 h), then heated to 800–1000 °C, and held for 1 to 48 h to reduce capsule porosity, stabilize the experiment, and mitigate the escape of sulfide liquid from the capsules along grain boundaries. After this sintering step, the temperature was raised to its nominal value at a heating rate of 100 °C/min and kept at run temperature for 20–360 min (Table 2). Experiments were quenched by shutting off electrical power, which causes a drop in temperature to < 80°C within 2–3 s (logged by the Eurotherm temperature controller).

The multi-anvil press was calibrated at room temperature using the change in electrical resistivity of Bi I–II (2.55 GPa, Bean et al. (1986)), Bi III–V (7.7 GPa – Bean et al.
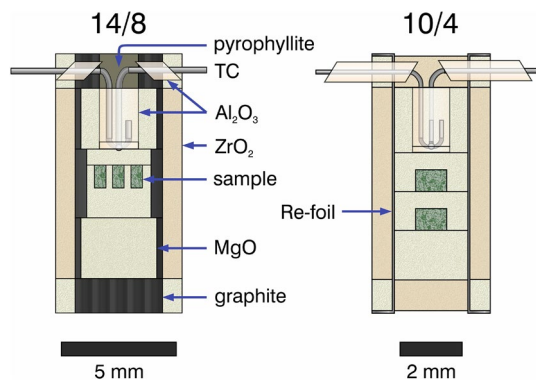
Fig. 3 Sketches of the central section of high-pressure assemblies used for high-pressure experiments between 6 and 14 GPa

(1986)), Zr $\alpha - \omega$ (7.96 GPa–Tange et al. (2011)), Pb I–II (13.4 GPa)(Bean et al. 1986), and ZnS (15 GPa – Piermarini and Block (1975)) using 4-wire sensing. The pressure calibration at temperature was done using the following phase transitions: $CaGeO_3$ (garnet–perovskite, 1200 °C, 5.61 GPa), SiO_2 (coesite–stishovite, 1200 °C, 9.27 GPa) and the olivine–wadsleyite (Stixrude and Lithgow-Bertelloni 2011) and olivine–ahrsenite (Chanyshev et al. 2021) binary loop at 1200 and 1400 °C. The pressure calibration was complemented by a temperature calibration using the melting curve of silver (Errandonea 2010) and gold (Akella and Kennedy 1971). We corrected the temperature offset between the thermocouple and sample based on the thermal model of our assemblies (Hernlund et al. 2006) and the average thermocouple distance to the sample, measured post-run. Thus, we applied a correction of + 40 °C to the temperature of the 10/4 experiments and + 20 °C to the temperature of the 14/8 experiments. Any effects of pressure on the electromotive force (emf) of the thermocouple were not considered.

Experiments at 2 GPa were carried out in an end-load piston cylinder apparatus (*Voggenreiter Mavopress LPC 250/30*), using standard 1/2" talc-Pyrex pressure assemblies wrapped in 0.025 mm lead-foil to minimize friction. Experiments were carried out using the hot-piston in method, where the sample was first taken to 90% of the target pressure, and subsequently heated to 800 °C. Samples were kept at 800 °C overnight, to sinter the capsule and reduce porosity, mitigating any potential loss of sulfide melt during the experiment. Subsequently, the temperature was raised 100 °C below its target, and then, pressure and temperature were simultaneously raised to the final run conditions, dwelt for some time (see Table 2), and terminated by shutting off the electrical power to the heater.

Pressure was previously calibrated using the albite breakdown reaction at 900 °C (Holland 1980), and the quartz–coesite phase transition at 1000 °C (Bose and Ganguly 1995). A friction correction of 20 % was applied

to the nominal pressure. The temperature was monitored using a type-D thermocouple, insulated by a corundum sleeve. A hollowed conic pyrophyllite plug was added at the point at which the corundum insulator intercepts the steel plug atop the pressure assembly. This step mitigated the extrusion of the thermocouple during compression and relaxation of the pressure assembly due to friction with the pressure vessel, which could otherwise lead to unreliable temperature monitoring during the experiment.

Complementary experiments were carried out at 0.1 MPa, using each of the four bulk compositions, to obtain constraints of the sulfide phase relationships at atmospheric pressure. In a similar fashion to the synthesis of each bulk composition, sample powders were evacuated at 1 Pa inside SiO_2 sealed glass tubes and reacted between 920 and 1220 °C using two $MoSi_2$-powered high-temperature furnaces (*Nabertherm LHT17*). The temperature was closely monitored by placing a Type-B thermocouple within 20 mm of the alumina crucibles containing the vacuum-sealed SiO_2-glass tubes. The temperature was found to be stable within 3 °C from the set temperature over the course of the experiment. Experiments were quenched by quickly removing them from the oven and then dropping them into a beaker filled with cold water.

Experimental samples were subsequently embedded into epoxy and ground longitudinally to reveal a cross-section of the sample. A succession of epoxy-bound diamond sanding plates and hard polishing discs with diamond paste, down to 1 µm, yielded the best results in terms of the quality of the polished surfaces. All samples were stored in a desiccator to prevent oxidation of the exposed sulfides.

Analytical methods

Experimental run products, and their textural properties, were characterized by means of optical microscopy and electron microscopy using a *JEOL JSM-7200F* SEM at the Center for Interface-Dominated High-Performance Materials (ZGH) of the Ruhr-University Bochum (Germany). A *JEOL 8530F* Field-Emission Electron Microprobe (EMPA), hosted at the Institute for Mineralogy of the University of Münster (Germany), was used to measure the major element composition of the different sulfide phases present in each experiment. Samples were measured with 15 kV and 15 nA using a 1–20 µm-diameter beam. The larger diameters were used to account for the heterogeneity of the quenched sulfide melts. Pyrite, chalcopyrite, and pentlandite were used as reference materials for S, Fe, and Ni. Periclase was used as reference material for O. The detection limit for O at the given analytical conditions was 0.1 wt.%.

Results

Experimental run products

In this study, we present the results of 66 experiments carried out at pressures between 0.1 MPa and 14 GPa in either a box furnace (0.1 MPa), a piston cylinder (2 GPa) apparatus and a multi-anvil press (6 - 14 GPa). A summary of experimental conditions, the capsule material used, and phases present in each experiment are given in Table 2.

Experimental run products consist of monosulfide solid solution (mss) and sulfide melt (L) depending upon pressure, temperature, and bulk composition. For E1, the bulk composition with the lowest Ni concentration of 6.3 wt.% and M/S of 0.91, we also observed close to idiomorphic $(Fe,Ni)S_2$ grains at pressures of 8 and 14 GPa. The composition and stoichiometry of the phase is close to that of pure pyrite (FeS_2). The peridotitic compositions did not precipitate FeS_2 except for composition P1 (M/S = 0.92) at 14 GPa, where idiomorphic FeS_2 grains coexist with sulfide melt. Note that the precipitate is found in the nominally colder part of the sample capsule, i.e., slightly off from the geometric center of the heater (Fig. 3). In some experiments, no distinct melt phase was observed, but the mss showed a deficit in Cu and Ni and an excess of Fe when compared to the bulk composition. This, coupled with the observation of sulfides along the grain boundaries of the capsule material (e.g., Electronic Annex Fig. 1), has led us to conclude that a melt fraction escaped from the capsule interior, leaving mss behind. The escaped sulfide melt pockets were too small to be measured using EMPA. This feature of our experiments mirrors similar observations made by Zhang and Hirschmann (2016) for some of their experiments, and we adopt their criteria and consider these experiments as having had coexisting mss and sulfide melt at run temperature and pressure.

Mss crystallized to massive polygonal grain aggregates, characteristic of sub-solidus crystallization, which showed varying diameters (10–100s µm) and homogeneous chemical composition, irrespective of the bulk composition and the relative position in the sample chamber. Quenched sulfide melts showed, however, two different textures. The so-called "typical" texture consists of a matrix with Ni-, Cu-depleted roundish grains and an interstitial sulfide that is enriched in Ni and Cu. This texture is unequivocally identified with a reflected light microscope and SEM (Fig. 4). In addition, we observed a sulfide melt texture that is much harder to identify. This "atypical" texture looks similar to mss at the first glance (Fig. 5), but the apparent grain boundaries have a curved shape, in contrast to the polygonal nature of mss. The interstitials are decorated with a micron-sized layer of another sulfide phase.
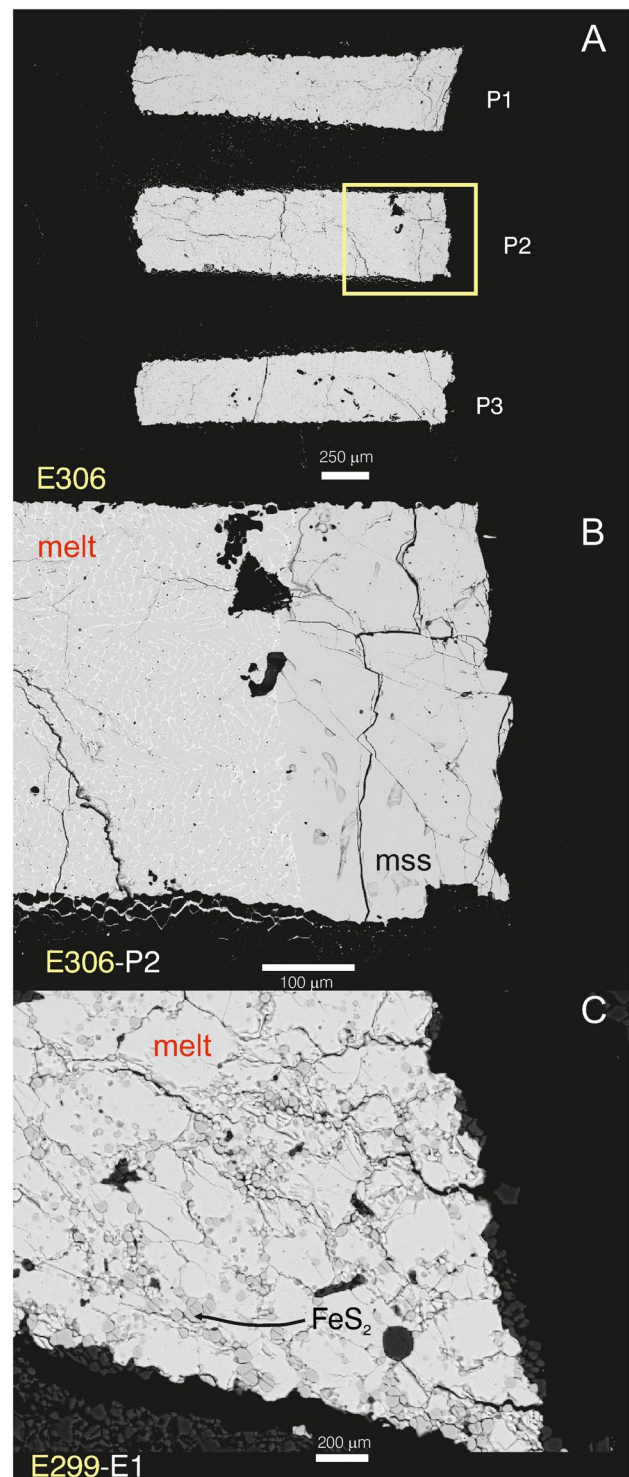

Fig. 4 Backscatter electron (BSE) images of typical experimental run products. **A** Overview of a 14/8 multi-capsule multi-anvil experiment (E306), where three identical compositions were run simultaneously. **B** Detail of experiment E306, composition P2, where both mss and sulfide liquid are clearly visible. **C** Example of sulfide melt from experiment E299, composition E1, carried out at 14 GPa, where liquidus pyrite(FeS_2) is present. mss = monosulfide solid solution, iss = intermediate sulfide solid solution, L = melt, ol = San Carlos olivine
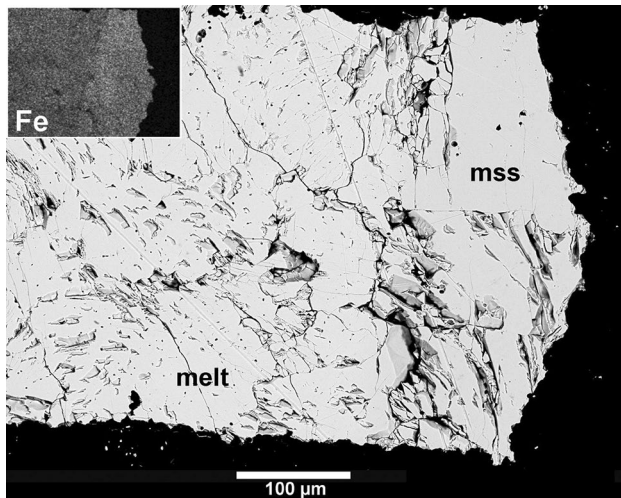
Fig. 5 BSE image of the P2 chamber of run E305 (8 GPa, 1270 °C) showing atypical sulfide melt coexisting with mss. The insert depicts the Fe K-series X-ray map and emphasizes the compositional difference between mss and melt

Fig. 6 Mineral-melt partitioning coefficients (D) between mss and sulfide melt. The data of Zhang and Hirschmann (2016) are shown for comparison. The propagated uncertainties are within the size of the symbols

Because the electron density contrast in the BSE images between the matrix and the interstitial phase is sometimes very low and the width of the interstitial phase is below one micron, the texture was initially misinterpreted as being mss. In samples with mss and atypical sulfide melt, we confirmed our observations by collecting Fe, Ni, and Cu X-ray maps for every experiment. The element maps revealed a distinct difference in the composition of the mss (Ni-poor, Fe-rich) and the coexisting melt (Ni-rich, Fe-poor), as well as a sharp boundary between both phases (Fig. 5). Another indicator that the atypical texture is different from sub-solidus mss is its response to polishing. Mss grains usually break off at the corners and thus have a tendency to break out during polishing. The mechanical response to the polishing of the atypical sulfide melt is very similar to that shown by their typical counterparts, which yield a smooth surface finish with fewer cavities than regions consisting of mss. This observation highlights the difficulties in clearly identifying mss and sulfide melt in experiments carried out at high pressure, which may obscure their phase relations.

Chemical composition of the sulfide phases

Two distinct mineral-melt partitioning trends for the mss and sulfide melt as a function of Ni content of the melt were observed, which have been also previously reported and discussed in great detail in earlier studies (e.g., Zhang and Hirschmann (2016), Bockrath et al. (2004)). The sulfide melt is enriched in Ni and Cu, whereas the coexisting mss is enriched in Fe, relative to the bulk composition (Fig. 6). Sulfur is close to evenly distributed between mss and melt.
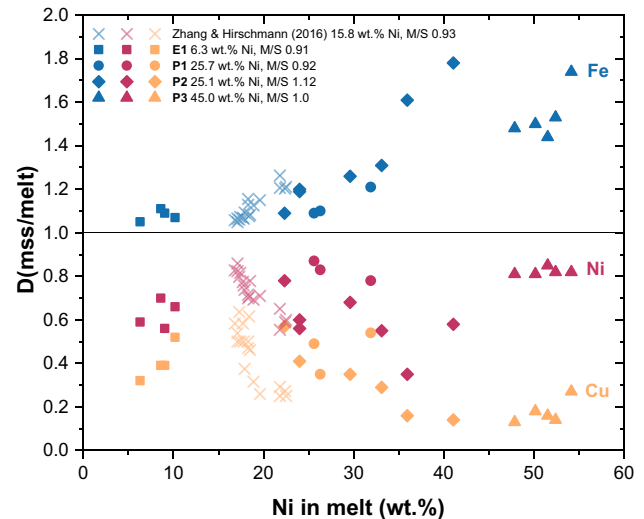
We see a disparity in the mineral-melt partitioning coefficients for Fe, Ni, and Cu between the Ni-poor composition and the three peridotitic Ni-rich compositions (P1, P2, P3). $D_{Cu}^{mss/melt}$ decreases between 20 and 35 wt.% Ni-in-melt and remains constant for higher Ni concentrations. The P2 and P3 compositions show decent agreement with the trend obtained by Zhang and Hirschmann (2016) for intermediate values of Ni-in-melt of 20 to 30 wt.%. The Ni-poor composition E1 (6.3 wt.% Ni) displays no obvious trends for $D_{Fe}^{mss/melt}$ and $D_{Ni}^{mss/melt}$. Only $D_{Cu}^{mss/melt}$ increases from 0.32 to 0.52 over a Ni-in-melt interval from 6.3 to 10.2 wt.%. The combined datasets are too small to extract any obvious effect of temperature or pressure on the mineral-melt partitioning coefficients. The full set of chemical data is given in the Electronic Annex Table 1. The O contents for about a third of the experiments are below the detection limit of 0.1 wt.%. 47 experiments have O concentrations above the detection limit, with a median of 0.16 wt.% and a standard error of 0.03 wt.%. The highest O concentrations of 0.94(6) wt.% were measured in sulfides encapsulated in silicate glass ampules that were used for the 0.1 MPa experiments.

Discussion

Solidi and liquidi calculation

To calculate the solidi and liquidi curves for each bulk composition, we employed the model proposed by Kechin (2001), which is based on the Simon equation for melting complemented by a dampening term (Eq. 1) (Fig. 7) to fit
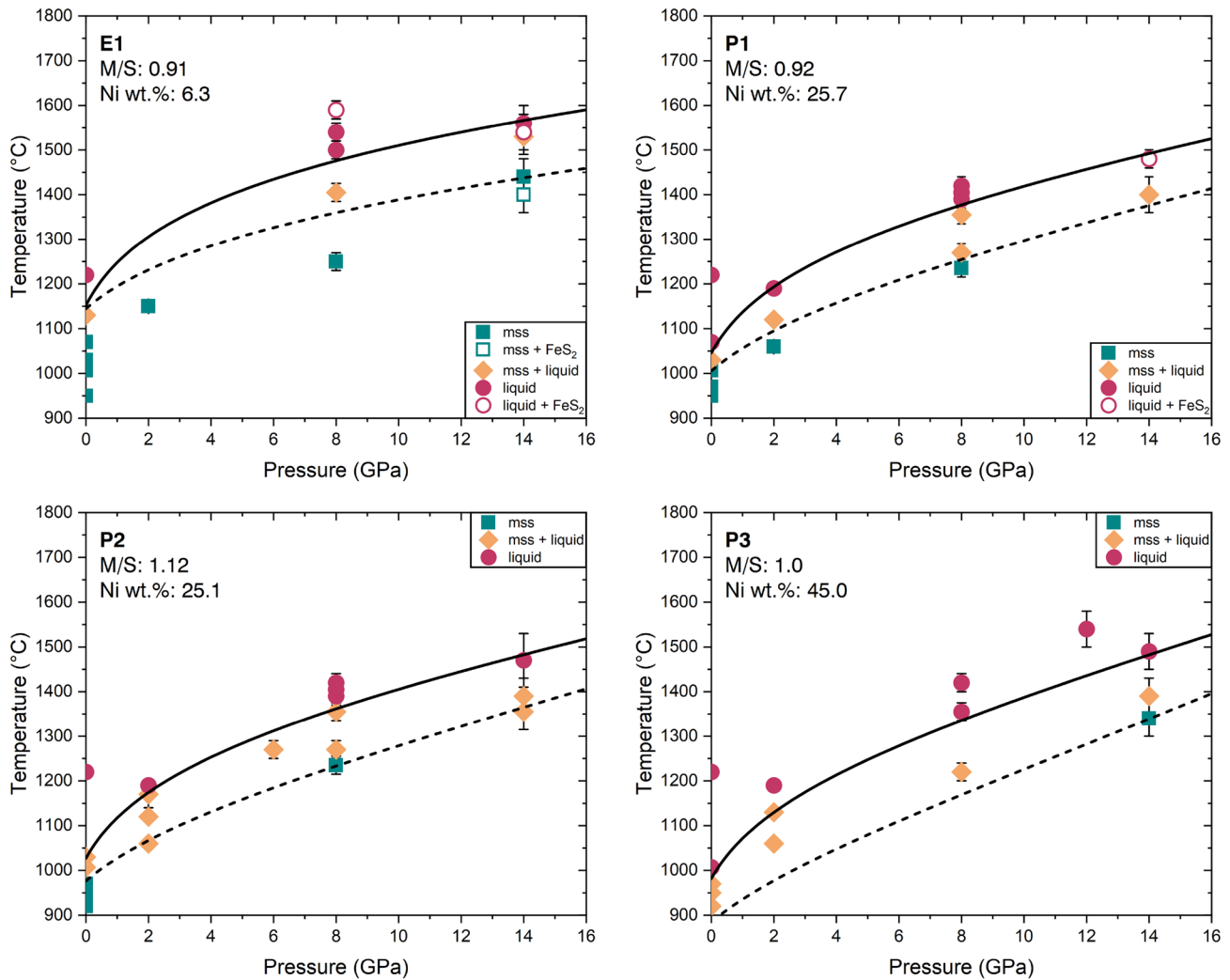
Fig. 7 Phase relations of the sulfide bulk compositions used in this study. The dashed line represents the solidus, and the solid line the liquidus. The liquidi and solidi curves are calculated using the modified Simon equation (Eq. 1) and the parameters given in Electronic Annex Table 2. The experimental temperatures are corrected for the modeled thermocouple offset, as discussed in the Methods section

each curve through temperature brackets that are defined by our experiments. *A priori*, we used only the narrowest bracket for each pressure. Brackets were weighted by their width, e.g., 35 °C for the bracket 1390–1355 °C. The accuracy of the curves was improved by experiments that contain only traces of mss or sulfide melt, implying that these experiments were close to their solidi and liquidi, respectively. Equation 1 was modified to take into account the effect of Ni and M/S on the melting curves to calculate the solidi and liquidi curves within the Fe–Ni–S system (Eqs. 1, 2). We followed the approach of Hirschmann (2000) and used a penalty function to fit a set of discrete observations, i.e., melt and no melt, and minimized the objective function by means of least-squares regression. Our experiments, namely those whose data were used to bracket the liquidus of each bulk composition, were combined with the experimental data set of Zhang and Hirschmann (2016).

The solidus curves were fitted based on our results only, and thus, the solidus is less well constrained compared to the liquidus (median bracket width: liquidus: 35 °C, solidus: 60 °C, and data density (number of data points: liquidus: 50 pts, solidus 27 pts). We have not used the Zhang and Hirschmann (2016) or Ballhaus et al. (2006) solidi, because we see a discrepancy in the shape and slope that is outside the range of typical experimental and analytical uncertainties. The discrepancy between the different solidi is best explained by the sensitivity of the solidus to the bulk starting M/S. Minor shifts of the M/S cause substantial variations in the solidus temperatures if the M/S of the bulk composition of the sulfide starting mix is close to 0.96, where pure FeS melts congruently (Waldner and Pelton 2004). As such, even
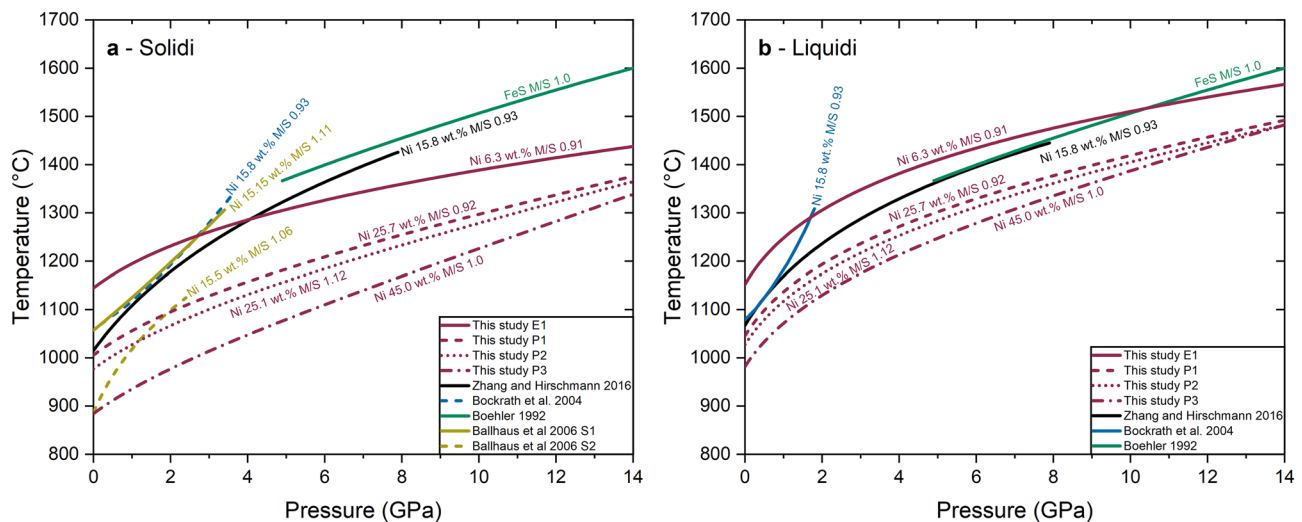
Fig. 8 Melting relations from previous sulfide experiments and results from this study. **a** Comparison of solidi. **b** Comparison of liquidi. Our data are plotted together with previous studies on the melt-ing curve of troilite (Boehler 1992) and mss (Bockrath et al. 2004; Ballhaus et al. 2006; Zhang and Hirschmann 2016)

small differences in the M/S between the bulk compositions studied here and those of Zhang and Hirschmann (2016) or Ballhaus et al. (2006) lead to large variations in the slope and shape of the respective solidi

$$T_{model}(°C) = T_{ref} \times \left[\frac{P}{a} + 1 \right]^b \exp[-cP(M/S)Ni] \quad (1)$$

with

$$T_{ref}(°C) = m((M/S)Ni)^2 + n((M/S)Ni) + 1196, \quad (2)$$

where T_{ref} is the solidus/liquidus temperature at 0.1 MPa, P is the pressure in GPa. A, b, and c are fitting parameters that are related to the volume change and enthalpy at the reference pressure (c.f. Eqs. 14–19, Kechin (2001)): M and n are empirical fitting parameters. M/S is the metal-to-sulfur ratio and Ni is the Ni content of the bulk composition in wt.%. We used the melting point of troilite (1196 °C) (Boehler 1992) and the liquidus/solidus of αNiS (976 °C / 807 °C) (Kullerud and Yund 1962) as boundary conditions to calculate the effect of Ni and M/S on the melting temperature along a hypothetical FeS - αNiS binary. The fitting parameters are given in Electronic Annex Table 2.

Using the fitted Eqs. 1 and 2, we calculated the liquidi of base metal sulfides in the system Fe–Ni–S between 6.3 and 45 wt.% Ni and for an M/S between 0.92 and 1.12, to cover the variability seen in diamond inclusions (Fig. 2). Because of the experimental bracket width and temperature uncertainties of the individual experiments, we estimated that the uncertainty of the liquidi is within 20 °C below 3 GPa, and within 30 °C between 3 and 14 GPa. As a result of the lower

data density and wider experimental brackets, we estimated the accuracy of the solidus to be 25 °C below 3 GPa, and 40 °C between 3 and 14 GPa.

Effect of bulk composition on the solidi and liquidi of base metal sulfides

The solidus and liquidus temperatures of all four bulk compositions rise monotonously with increasing pressure (Fig. 7). Melting temperatures vary primarily with the Ni content of the bulk composition and to a lesser extent with the M/S within the studied compositional spectrum (Fig. 8). The difference in the solidi and liquidi for the different bulk compositions is most significant at 0.1 MPa. The relative temperature difference between both curves is roughly constant with increasing pressure up to ∼6 GPa. At pressures above 6 GPa, the melting curves from all compositions start to converge. The liquidus temperatures for the peridotitic compositions are almost identical above 11 GPa within the uncertainties of the experimental data. Eclogitic sulfide (E1) with 6.3 wt.% Ni and the Ni-rich, peridotitic sulfide (P3) with 45 wt.% Ni, which are the compositions with the largest difference in their Ni content, exhibit a difference in the liquidus temperatures as large as 170 °C at 0.1 MPa. The difference decreases significantly with increasing pressures and is reduced to 84 °C at 14 GPa (Fig. 8a). A similar trend is mimicked for the solidus curves, as shown in Fig. 8b, although the convergence between E1 and P3 is not as clear as it is for the liquidus curves. Overall, Ni-poor compositions are more refractory than Ni-rich compositions.

For the time being, we have no definitive explanation for why the curves begin to converge around 6 GPa. As a basis for further discussion, we refer to the study of Urakawa et al. (2004), where the authors identified a spin transition in the high-pressure and high-temperature FeS V phase from a low-pressure high-spin phase (LPP) to a high-pressure low-spin phase (HPP). The spin transition starts at around 7 GPa
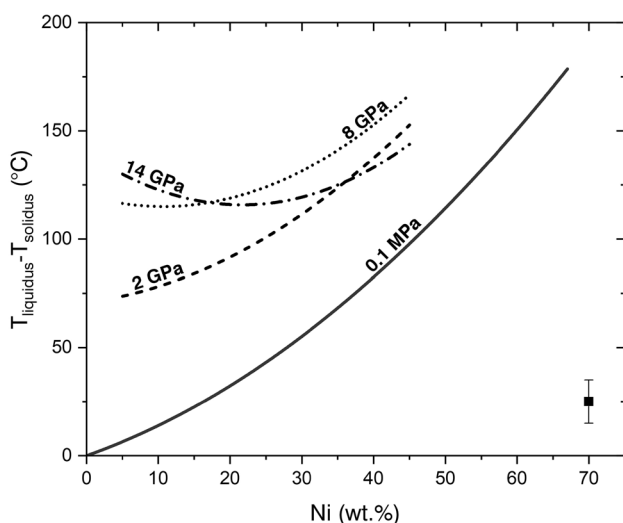

Fig. 9 $\Delta T = T_{liqidus} - T_{solidus}$ calculated using Eq. 1 shown as a function of Ni (wt.%), in the system Fe–Ni–S. The M/S was fixed to 1. ΔT at 0.1 MPa and 0 wt.% Ni and 67.4 wt.% Ni are based on the melting temperatures given by Boehler (1992) and Kullerud and Yund (1962). The uncertainty displayed in the lower right corner represents an average uncertainty of 20 °C

and ends at 12 GPa for pure FeS V at 927 °C. The transition is accompanied by an abrupt change in the unit cell volume and anomalous behavior in the thermal expansivity in the transient region between 4 and 9 GPa. The pressure interval coincides with the observed change in the melting curve. If this behavior is also persistent in $Fe_{(1-x)}S–Ni_{(1-x)}S$ solid solutions, the change in the thermoelastic properties may affect mineral-melt partitioning and phase relations involving mss (Urakawa et al. 2004). As such, we consider it plausible that this change in spin state and molar volume of mss will affect the shapes of the melting curves above 6 GPa as observed in our experiments.

By examining the width (i.e., the temperature range) of the mss plus melt two-phase field, which is bounded by the solidus and liquidus ($\Delta T = T_{liqidus} - T_{solidus}$), we found a positive correlation between Ni and the dimensions of the two-phase field at a given pressure (Fig. 9). The observations made at 0.1 MPa are readily explained by superimposing our results on the Fe–Ni–S ternary and the Fe–S and Ni–S binary phase diagrams at 0.1 MPa (Raghavan 2004; Waldner and Pelton 2004, 2005). For compositions with M/S above the congruent mss composition (~52 at.% S or M/S = 0.96 in the Fe–S system), the width of the two-phase field decreases with increasing M/S towards the eutectic of the Fe-rich portion of the phase diagram. This trend is mirrored for compositions with M/S below 0.96, i.e., on the S-rich side of the congruent melting point. E1's composition is close to the congruent melting point of pyrrhotite ($Fe_{(1-x)}S$), which explains the narrow melting interval of 9 K. Overall,
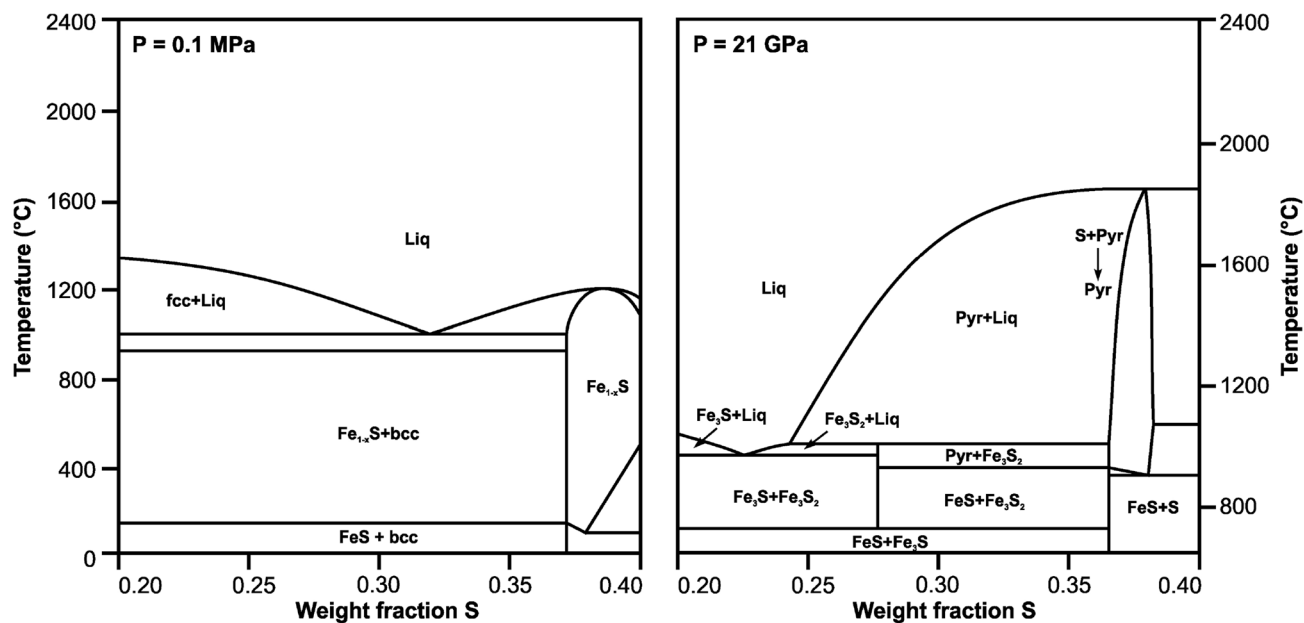

Fig. 10 (Left) T–X phase diagram in the system Fe–S modified after Waldner and Pelton (2004). (Right) Phase diagram of the Fe–S system modified based on Fig.2 of Saxena and Eriksson (2015). *fcc* face-centered cubic iron, *liq* melt, *pyr* pyrrhotite

our results agree with the phase diagrams calculated at 0.1 MPa (Fig. 10).

With increasing pressure, the two-phase field becomes wider for a given Ni content and M/S. The ΔT increases with increasing pressure for Ni of up to 15 wt.%. This is in good agreement with the Fe–S binary, modeled at high-pressures (cf. Saxena and Eriksson 2015, Fig. 10). For Ni contents larger than 15 wt.%, ΔT peaks between 6 and 8 GPa and then decreases slightly with increasing pressure. Compared to the effect of Ni on ΔT at pressures below 2 GPa, ΔT becomes less sensitive to changes in the Ni content of mss at higher pressures. This implies that with increasing pressures, relative differences in the thermoelastic properties of the different end-member components (e.g., thermal expansivity and K'), as well as molar volume, that could affect phase relations are probably mitigated.

Comparison to previous work

The solidi obtained in this study are not in agreement with those published by Ballhaus et al. (2006), Bockrath et al. (2004) and Zhang and Hirschmann (2016). Our solidi are significantly shallower and are less concave. If we consider the phase diagram calculated by Saxena and Eriksson (2015) and compare the expanse of the two-phase field at 21 GPa with the expanse of the two-phase field at 0.1 MPa (Waldner and Pelton 2004), the width of the field increases from 190 to 400 ° C for a mss with M/S of 1. The expansion of the two-phase field is reflected in our data. Note that the width is extremely sensitive to M/S for compositions that are close to the congruent melting point of $Fe_{(1-x)}S$, which might explain the discrepancy between the solidi of Bockrath et al. (2004) and Zhang and Hirschmann (2016) and our own solidi data. Another reason why our solidi are less concave is the limited number of solidus observations at high pressures that are required to better constrain the curvature of the solidus over the studied pressure interval that was covered by our experiments (i.e., 0.1 MPa to 14 GPa).

We also compared our model with the tightly bracketed solidus (1175 °C–1185 °C) at 1.5 for a Ni-poor composition (Li and Audétat (2012), cf. composition S03), similar to E1. The experiments were buffered in terms of oxygen fugacity to values between − 1.0 and 0.7 log units relative to the fayalite–magnetite–quartz (FMQ) buffer. Using our model, we calculated the solidus for this composition to be 1215(25) °C. Given the differences in Ni content (6.1 wt.% for E1 and 7.06 wt.% for S03) and the higher O content of the crystallized phases (< 0.1 wt.% to 0.14(2) wt.% for E1 and 0.4(2) to 1.0(7) wt.% for S03), the calculated solidus is in very good agreement to the experimental bracket.

The liquidi fitted to the experiments conducted by Bockrath et al. (2004) and Zhang and Hirschmann (2016) for an mss with 15.8 wt.% Ni and M/S 0.93 broadly agree with our trends up to 1 GPa (Fig. 8). At higher pressures, the Bockrath et al. (2004) liquidus becomes convex with pressure, as opposed to our results and those of Zhang and Hirschmann (2016), which yield concave liquidi. Also, the Bockrath et al. (2004) liquidus crosses the liquidus of pure pyrrhotite around 3 GPa, which is unrealistic as FeS is the most refractory component of the Fe–Ni–Cu–S system (see discussion in Zhang and Hirschmann (2016)). The more recent liquidus curve of Zhang and Hirschmann (2016) has a similar curvature to the liquidi obtained for the bulk compositions used in this study. The E1 liquidus is above the melting curve of troilite (Boehler 1992) below 10 GPa, but has a similar shape. Given the reported uncertainties of both experimental studies and the imperfections of the fitting, the curves are still in decent agreement. As discussed in the previous section, we partially attribute the discrepancy between the melting curve of pure FeS and the liquidus of E1 to their difference in M/S. We see a similar depression of the liquidus for compositions P1 (M/S = 0.92) and P2 (M/S = 1.12), where the P1 liquidus is at higher temperatures than that of P2, in accordance with previous observations that higher M/S lead to a depression in the liquidus (Ballhaus et al. 2006).

Although our experiments were not nominally buffered, comparing our O contents to the experiments of Zhang et al. (2018) for which the authors provide constraints on the oxygen fugacity based on the Mg# and Fe diffusion profiles in coexisting olivine, we estimate the oxygen fugacity of our experiments between FMQ-2 and FMQ-4 (Electronic Annex Fig. 2). Thus, our experiments were largely reduced with oxygen fugacities that are within the range of what has been proposed for the lithospheric and sub-lithospheric mantle (Frost and McCammon 2008).

Implications for the mobility of chalcophile elements and the formation of diamonds in the earth's upper mantle

Sulfides are the major reservoir for chalcophile elements, e.g., HSE, Au, Ag, and Pb in the Earth's mantle (e.g., Liu and Brenan (2015)). Intriguingly, eclogitic sulfides, here represented by the Ni-poor (6.3 wt.% Ni) composition E1, are mostly solid along continental geotherms with a surface heat flow of 30 to 50 mW/m², which are typical values for the cratonic lithosphere (Fig. 11). A recent study on the protogenetic nature of eclogitic sulfide inclusions in diamonds from the Victor and Jericho kimberlite (Canada), with a calculated average mss composition of $Fe_{0.84(3)}Ni_{0.07(4)}Cu_{0.02(1)}$
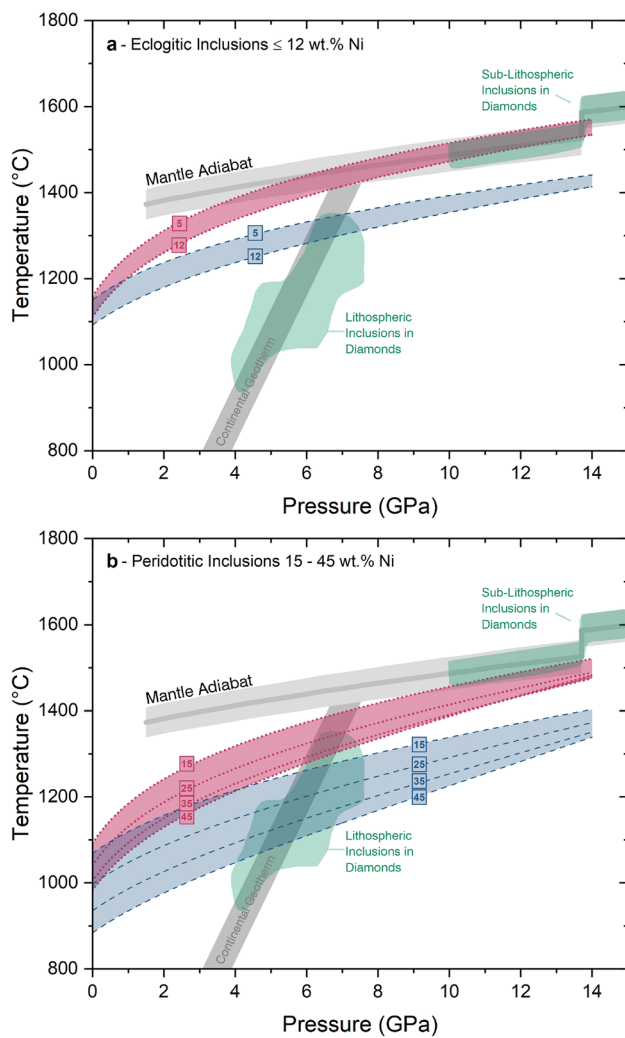
Fig. 11 **a** Pressure–temperature diagram showing a range of calculated solidi and liquidi for eclogitic inclusions with a bulk Ni concentration of 5–12 wt.% plotted against continental geotherms with a surface heat flow of 30 to 50 mW/m^2 following Sclater et al. (1980) and the mantle adiabat with a mantle potential temperature of 1350 °C (Katsura 2022). The field of lithospheric inclusions is from Stachel and Harris (2008) and the field of sub-lithospheric diamonds is taken from Beyer and Frost (2017) and references therein, projected onto the mantle adiabat. Note that the pressure and temperature of the inclusions are based on geothermobarometry of silicates and do not represent the pressure and temperature of the sulfides. Thus, the areas need to be understood as the range of possible pressures and temperatures for inclusions in diamonds. **b** Same pressure–temperature diagram as given in Fig. 11a, but the liquidus and solidus for Ni-rich, peridotitic sulfides are shown. The range of Ni contents of the mss is between 15 wt.% and 45 wt.%. All solidus and liquidus curves were calculated for an M/S of 1.0

S$_{1.0}$, supports our findings that eclogitic sulfides remain solid within the cratonic lithosphere (Pamato et al. 2021). Only at pressures above 6 GPa and temperatures above 1250 °C,

eclogitic sulfides will begin to melt incongruently, within the pressure/temperature stability field of lithospheric diamonds. Accordingly, such low-Ni sulfides will fractionate chalcophile elements only at greater depths and/or higher temperatures. At pressures corresponding to the sub-lithospheric mantle, i.e., above 9 GPa, eclogitic sulfides are partially molten and will only become fully molten when the sulfide liquidus crosses the mantle adiabat at around 14 GPa. From this melting behavior, we can draw two conclusions. First, the fractionation of chalcophile elements in eclogitic sulfides is restricted to a pressure interval of 6 to 14 GPa along a cratonic mantle geotherm and the mantle adiabat. Second, eclogitic sulfide inclusions found in diamonds formed at pressures below 6 GPa are protogenetic crystalline sulfides, entrapped by the diamond-forming fluid, whereas sulfides found in diamonds that formed at higher pressures probably represent partially or fully molten sulfides. These melts would then have a syngenetic relationship to the diamond-forming fluid. This partial sulfide melt will fractionate chalcophile elements and will leave a Ni- and Cu-depleted restite behind.

In contrast to our findings on Ni-poor compositions, our data on peridotitic sulfides with Ni > 15 wt.% show that Ni-rich sulfides are partially molten throughout nearly the entire pressure/temperature stability field of lithospheric inclusions in diamonds, which agrees with the findings of Zhang and Hirschmann (2016). However, we disagree that peridotitic sulfides may become crystalline again in the deeper mantle, because, based on our results, the liquidus and solidus of peridotitic sulfides do not cross the mantle adiabat in the sub-lithospheric mantle (Fig. 11). Zhang and Hirschmann (2016) interpretation is based on the extrapolation of their regression curves above 8 GPa, whereas our data cover an extended pressure regime of up to 14 GPa. Consequently, we propose that sulfide inclusions found in sub-lithospheric diamonds have likely formed syngenetic and are remnants of entrapped sulfide melts. However, any addition of carbon or oxygen will depress the solidus temperature by up to 80 °C and will aid the formation of sulfide melts (e.g., Urakawa et al. (1987); Zhang et al. (2015)).

Several recent studies by Aulbach et al. (2017, 2019), as well as Smart et al. (2017) have proposed that the oxygen fugacity of Archean eclogites in cratonic settings, namely those that are diamond-bearing, to be between FMQ-1 and as low as FMQ-4, which reflects the conditions of our experiments. Moreover, the transition to more metal-rich sulfide compositions by a reduction of oxygen fugacity with increasing pressure (Frost and McCammon 2008; Rohrbach and Schmidt 2011) will also decrease the melting temperature of sulfides. Thus, the results of our study mark the upper

Table 1 Compositions of the starting materials (nominal composition based on the weighted portions)

	Ions per formula unit				Weight%				M/S
	Fe	Ni	Cu	S	Fe	Ni	Cu	S	
P1	0.54	0.37	0.01	1.0	35.7	25.7	0.8	37.9	0.92
P2	0.70	0.41	0.01	1.0	40.8	25.1	0.7	33.5	1.12
P3	0.30	0.69	0.01	1.0	18.6	45.0	0.7	35.7	1.00
E1	0.81	0.09	0.01	1.0	54.4	6.3	0.8	38.5	0.91

ceiling in terms of sulfide melting temperatures with respect to the effect of carbon saturation (by diamond).

The assessment of the effect of carbon on sulfide solidi and how this impacts the significance of our data is more complicated. If we assume that the sulfide is in equilibrium with a carbon-bearing liquid from which the diamond precipitates, then we have to assume that the sulfide is carbon-saturated and the liquidus and solidus temperatures are correspondingly lower than the temperatures given in Fig. 11. Another possible scenario is that the sulfide formed protogenetic before it was entrapped during the diamond-forming process (i.e., redox-freezing of a carbonated silicate melt or C–O–H fluid). Only when the diamond-forming medium interacts with the sulfide/sulfide melt, may the sulfide become carbon-saturated, and an erstwhile solid crystalline sulfide might melt after entrapment. Interestingly, even though there are ample studies on the saturation of carbon in metal and sulfide melts with graphite as the carbon source (e.g., Zhang et al. (2015, 2018)), to our knowledge, no single study has investigated the carbon content of sulfides at diamond saturation, despite the fact that sulfides are common inclusions in diamonds. Assuming that diamond is the more stable phase at mantle P–T conditions, could this also mean that less carbon is dissolved in sulfides in the presence of diamonds? This question remains a conundrum for the time being and can only be addressed by further experimental or computational studies in the future. Regardless of the potential effect of C and O on the sulfide solidi, our data clearly show that Ni-poor sulfide inclusions are those most likely to remain crystalline in Earth's mantle, compared to Ni-rich inclusions, and that the effect of Ni content in sulfide is a key factor determining the P–T space covered by sulfide solidi.

Whether sulfide melt can escape from a crystalline silicate matrix and percolates through the mantle, depends upon the wetting properties of the melt, which largely hinge on the S and O contents of the sulfide melt (Gaetani and Grove 1999; Terasaki et al. 2005). For example, if eclogite formed from an average modern-day MORB with bulk $Fe^{3+}/\Sigma Fe$ of 0.16 (Cottrell and Kelley 2011), it has the potential to increase the O content of a coexisting sulfide liquid. Indeed,

at least at 0.1 MPa, sulfide may dissolve as much as 12 wt.% O at oxygen fugacities around the fayalite-magnetite-quartz redox equilibrium (cf., and references therein Fonseca et al. (2008)). Moreover, Walter et al. (2008) demonstrated that sub-lithospheric inclusions with a basaltic origin conserve an oxygen fugacity above the diamond stability field down to the lower mantle. Under the premise that the observations of Gaetani and Grove (1999) and Terasaki et al. (2005) can be applied to silicate assemblages comprised of majoritic garnet, clinopyroxene, and an olivine polymorph, then sulfide liquids have the potential to migrate and efficiently redistribute chalcophile elements within Earth's mantle. Indeed, the role of sulfide melt migration in promoting metasomatism in peridotites, and affecting their chalcophile element content, has been indicated in multiple studies (e.g., Luguet et al. (2008); Harvey et al. (2010)). However, if such a melt interacts with a reduced environment, e.g., depleted mantle domains, it will stop migrating and becomes trapped within the silicate matrix. This process of redox-freezing is already well known from C–O–H fluids (Rohrbach and Schmidt 2011).

Concluding remarks

We showed that without invoking the presence of C or O, Ni-rich sulfide melts are partially molten throughout the upper mantle, and are fully molten in the sub-lithospheric mantle. Ni-poor sulfides, i.e., eclogitic sulfides, however, are more refractory and barely melt in the cratonic mantle without the depression of their solidus by trace components such as C or O. Our data reveal that a more comprehensive knowledge of the effect of Ni/(Ni+Fe), and M/S, on the melting relationships of base metal sulfides is required to decipher the nature of sulfide inclusions in diamonds. Future studies might investigate the basic thermodynamic properties of base metal sulfides in the system $Fe_{(1-x)}S$–$Ni_{(1-x)}S$ at high pressures and high temperatures, taking into account the spin transition in Fe(Ni) sulfide, to establish

Table 2 Experimental conditions and run products

Experiment #	Pressure (GPa)	T (uncorrected) (°C)	T (corrected) (°C)	Duration (minutes)	Capsule	Phases
P1($Fe_{0.54}N_{i0.37}Cu_{0.01}S_{1.00}$)						
P1_ 2022_ 2	0.0001	950	950	5670	SiO_2	mss
P1_ 970	0.0001	970	970	2540	SiO_2	mss
P1_ 1007	0.0001	1007	1007	4020	SiO_2	mss
L86	2	1050	1060	70	MgO	mss
E302	8	1215	1235	90	MgO	mss
P1_ 1030	0.0001	1030	1030	2420	SiO_2	mss + L
L87	2	1110	1120	30	MgO	mss + L
E305	8	1250	1270	60	MgO	mss + L
E306	8	1335	1355	60	MgO	mss + L
E315	14	1360	1400	20	MgO	mss + L
P1_ 1070	0.0001	1070	1070	2640	SiO_2	L
P1_ 2022_ 1	0.0001	1220	1220	5670	SiO_2	L
L84	2	1180	1190	120	MgO	L
E307	8	1370	1390	60	MgO	L
E308	8	1400	1420	120	MgO	L
E309	8	1385	1405	150	MgO	L
E326	14	1440	1480	60	MgO	L + FeS_2
P2($Fe_{0.70}N_{i0.41}Cu_{0.01}S_{1.00}$)						
P2_ 920	0.0001	920	920	4050	SiO_2	mss + iss
P2_ 2022_ 2	0.0001	950	950	4050	SiO_2	mss
E302	8	1215	1235	90	MgO	mss
P2_ 970	0.0001	970	970	2540	SiO_2	mss+ L
P2_ 1007	0.0001	1007	1007	4020	SiO_2	mss + L
P2_ 1030	0.0001	1030	1030	2420	SiO_2	mss + L
L87	2	1110	1120	30	MgO	mss + L
E228	6	1250	1270	120	SC ol	mss + L
E305	8	1250	1270	60	MgO	mss + L
E306	8	1335	1355	60	MgO	mss + L
E313	14	1315	1355	60	MgO	mss + L
E314	14	1350	1390	34	MgO	mss + L
P2_ 2022_ 1	0.0001	1220	1220	1150	SiO_2	L
L84	2	1180	1190	120	MgO	L
E307	8	1370	1390	60	MgO	L
E309	8	1385	1405	150	MgO	L
E308	8	1400	1420	120	MgO	L
E312	14	1420	1470	30	SiO_2	L
P3($Fe_{0.30}Ni_{0.69}Cu_{0.01}S_{1.00}$)						
E319	14	1300	1340	50	MgO	mss
P3_ 920	0.0001	920	920	4050	SiO_2	mss + L
P3_ 2022_ 2	0.0001	950	950	5670	SiO_2	mss + L
P3_ 970	0.0001	970	970	2540	SiO_2	mss + L
L87	2	1120	1130	30	MgO	mss + L
L82	2	1120	1130	30	MgO	mss + L
E324	8	1200	1220	120	MgO	mss + L
E314	14	1350	1390	34	MgO	mss + L
P3_ 1007	0.0001	1007	1007	4020	SiO_2	L
P3_ 2022_ 1	0.0001	1220	1220	1150	SiO_2	L
L84	2	1180	1190	120	MgO	L
E306	8	1335	1355	60	MgO	L

Table 2 (continued)

Experiment #	Pressure (GPa)	T (uncorrected) (°C)	T (corrected) (°C)	Duration (minutes)	Capsule	Phases
E308	8	1400	1420	120	MgO	L
E272	12	1500	1540	150	SC ol	L
E321	14	1450	1490	40	SC ol	L
$E1(Fe_{0.81}Ni_{0.09}Cu_{0.01}S_{1.00})$						
E1_1007	0.0001	1007	1007	4020	SiO_2	mss
E1_1030	0.0001	1030	1030	2420	SiO_2	mss
E1_1070	0.0001	1070	1070	2640	SiO_2	mss
L91	2	1140	1150	120	MgO	mss
E233	8	1230	1250	360	SiO_2	mss
E323	14	1400	1440	30	SiO_2	mss
E1_1130	0.0001	1130	1130	4040	SiO_2	mss + L
E309	8	1385	1405	150	MgO	mss + L
E315	14	1360	1400	20	SiO_2	mss + FeS_2
E323	14	1400	1440	30	SiO_2	mss + FeS_2
E296	14	1490	1530	15	SiO_2	mss + L + FeS_2
E1_2022_1	0.0001	1220	1220	1150	SiO_2	L
E295	8	1480	1500	90	SiO_2	L
E297	8	1520	1540	60	SiO_2	L
E300	8	1570	1590	40	MgO	L + FeS_2
E299	14	1500	1540	60	MgO	L

mss monosulfide solid solution, *iss* intermediate sulfide solid solution, *SC ol* single crystal olivine, *L* = sulfide melt

a thermodynamic model that is applicable to the variance of base metal sulfides seen in Earth's mantle.

References

Akella J, Kennedy GC (1971) Melting of gold, silver, and copper-proposal for a new high-pressure calibration scale. J Geophys Res 76(20):4969–4977

Anderson O (1982) The earth's core and the phase diagram of iron. Philos Trans R Soc Lond Ser A 306(1492):21–35

Aulbach S, Creaser RA, Pearson NJ, Simonetti SS, Heaman LM, Griffin WL, Stachel T (2009) Sulfide and whole rock RE-OS systematics of eclogite and pyroxenite xenoliths from the slave craton, Canada. Earth Planet Sci Lett 283(1–4):48–58

Aulbach S, Woodland AB, Vasilyev P, Galvez ME, Viljoen K (2017) Effects of low-pressure igneous processes and subduction on fe3+/fe and redox state of mantle eclogites from lace (Kaapvaal craton). Earth Planet Sci Lett 474:283–295

Aulbach S, Woodland AB, Stern RA, Vasilyev P, Heaman LM, Viljoen K (2019) Evidence for a dominantly reducing Archaean ambient mantle from two redox proxies, and low oxygen fugacity of deeply subducted oceanic crust. Sci Rep 9(1):1–11

Ballhaus C, Bockrath C, Wohlgemuth-Ueberwasser C, Laurenz V, Berndt J (2006) Fractionation of the noble metals by physical processes. Contrib Miner Pet 152(6):667–684

Bean VE, Akimoto S, Bell PM, Block S, Holzapfel WB, Manghnani MH, Nicol MF, Stishov SM (1986) Another step toward an international practical pressure scale: 2nd AIRAPT IPPS task group report. Phys BC 139–140:52–54

Beyer C, Frost DJ (2017) The depth of sub-lithospheric diamond formation and the redistribution of carbon in the deep mantle. Earth Planet Sci Lett 461:30–39

Bockrath C, Ballhaus C, Holzheid A (2004) Fractionation of the platinum group elements during mantle melting. Science 305:1951–1953

Boehler R (1992) Melting of the FEFEO and the FEFES systems at high pressure: constraints on core temperatures. Earth Planet Sci Lett 111(2–4):217–227

Boehler R (1996) Fe-fes eutectic temperatures to 620 kbar. Phys Earth Planet Inter 96(2–3):181–186

Bolfan-Casanova N, Keppler H, Rubie DC (2000) Water partitioning between nominally anhydrous minerals in the mgo-sio$_2$-h$_2$o system up to 24 gpa: implications for the distribution of water in the earth's mantle. Earth Planet Sci Lett 182(3–4):209–221

Bose K, Ganguly J (1995) Experimental and theoretical studies of the stabilities of talc, antigorite and phase A at high pressures with applications to subduction processes. Earth Planet Sci Lett 136(3–4):109–121. https://doi.org/10.1016/0012-821X(95)00188-I

Bulanova GP, Griffin WL, Ryan CG, Shestakova OY, Barnes SJ (1996) Trace elements in sulfide inclusions from Yakutian diamonds. Contrib Miner Petrol 124(2):111–125

Bulanova GP, Walter MJ, Smith CB, Kohn SC, Armstrong LS, Blundy J, Gobbo L (2010) Mineral inclusions in sublithospheric diamonds from collier 4 kimberlite pipe, Juina, Brazil: subducted protoliths, carbonated melts and primary kimberlite magmatism. Contrib Miner Pet 160(4):489–510

Chanyshev A, Bondar D, Fei H, Purevjav N, Ishii T, Nishida K, Bhat S, Farla R, Katsura T (2021) Determination of phase relations of the olivine-ahrensite transition in the Mg2SiO4-Fe2SiO4 system at 1740 K using modern multi-anvil techniques. Contrib Minerol Petrol 176(10):77. https://doi.org/10.1007/s00410-021-01829-x

Chaussidon M, Albaréde F, Sheppard SMF (1987) Sulphur isotope heterogeneity in the mantle from ion microprobe measurements of sulphide inclusions in diamonds. Nature 330(6145):242–244

Cottrell E, Kelley KA (2011) The oxidation state of Fe in MORB glasses and the oxygen fugacity of the upper mantle. Earth Planet Sci Lett 305(3):270–282. https://doi.org/10.1016/j.epsl.2011.03.014

Dromgoole EL, Pasteris JD (1987) Interpretation of the sulfide assemblages in a suite of xenoliths from Kilbourne Hole, New Mexico. Mantle metasomatism and alkaline magmatism. Geological Society of America, Boulder. https://doi.org/10.1130/SPE215-p25

Eggler DH, Lorand JP (1993) Mantle sulfide geobarometry. Geochim Cosmochim Acta 57:2213–2222

Errandonea D (2010) The melting curve of ten metals up to 12 gpa and 1600 k. J Appl Phys 108(3):033517

Férot A, Bolfan-Casanova N (2012) Water storage capacity in olivine and pyroxene to 14 gpa: implications for the water content of the earth's upper mantle and nature of seismic discontinuities. Earth Planet Sci Lett 349:218–230

Fleet ME, Pan Y (1994) Fractional crystallization of anhydrous sulfide liquid in the system Fe–Ni–Cu–S, with application to magmatic sulfide deposits. Geochim Cosmochim Acta 58(16):3369–3377. https://doi.org/10.1016/0016-7037(94)90092-2

Fonseca ROC, Campbell IH, O'Neill HSC, Fitzgerald JD (2008) Oxygen solubility and speciation in sulphide-rich mattes. Geochim Cosmochim Acta 72(11):2619–2635

Frost DJ, McCammon CA (2008) The redox state of earth's mantle. Annu Rev Earth Planet Sci 36(1):389–420. https://doi.org/10.1146/annurev.earth.36.031207.124322

Gaetani GA, Grove TL (1999) Wetting of mantle olivine by sulfide melt: implications for Re/Os ratios in mantle peridotite and late-stage core formation. Earth Planet Sci Lett 169:147–163

Harvey J, Gannoun A, Burton K, Schiano P, Rogers N, Alard O (2010) Unravelling the effects of melt depletion and secondary infiltration on mantle Re-Os isotopes beneath the French Massif Central. Geochim Cosmochim Acta 74(1):293–320

Helmy HM, Ballhaus C, Wohlgemuth-Ueberwasser C, Fonseca ROC, Laurenz V (2010) Partitioning of Se, As, Sb, Te and Bi between monosulfide solid solution and sulfide melt - application to magmatic sulfide deposits. Geochim Cosmochim Acta 74:6174–6179

Hernlund J, Leinenweber K, Locke D, Tyburczy JA (2006) A numerical model for steady-state temperature distributions in solid-medium high-pressure cell assemblies. Am Miner 91(2–3):295–305

Hirschmann MM (2000) Mantle solidus: experimental constraints and the effects of peridotite composition. Geochem Geophys Geosyst. https://doi.org/10.1029/2000GC000070

Holland T (1980) The reaction albite= jadeite+ quartz determined experimentally in the range 600–1200. Am Miner 65(1–2):129–134

Katsura T (2022) A revised adiabatic temperature profile for the mantle. J Geophys Res 127(2):e2021JB023562

Kechin VV (2001) Melting curve equations at high pressure. Phys Rev B 65(5):052102

Kullerud G, Yund RA (1962) The Ni-S system and related minerals. J Pet 3(1):126–175. https://doi.org/10.1093/petrology/3.1.126

Li Y, Audétat A (2012) Partitioning of V, Mn, Co, Ni, Cu, Zn, As, Mo, Ag, Sn, Sb, W, Au, Pb, and Bi between sulfide phases and hydrous basanite melt at upper mantle conditions. Earth Planet Sci Lett 355:327–340

Liu Y, Brenan J (2015) Partitioning of platinum-group elements (PGE) and chalcogens (Se, Te, As, Sb, Bi) between monosulfide-solid solution (MSS), intermediate solid solution (ISS) and sulfide liquid at controlled fO$_2$-fS$_2$ conditions. Geochim Cosmochim Acta 159:139–161

Luguet A, Pearson DG, Nowell GM, Dreher ST, Coggon JA, Spetsius ZV, Parman SW (2008) Enriched Pt–Re–Os isotope systematics in plume lavas explained by metasomatic sulfides. Science 319:453–456

Naldrett AJ, Craig JR, Kullerud G (1967) The central portion of the Fe–Ni–S system and its bearing on pentlandite exsolution in iron-nickel sulfide ores. Econ Geol 62(6):826–847

Padrón-Navarta JA, Hermann J (2017) A subsolidus olivine water solubility equation for the earth's upper mantle. J Geophys Res 122(12):9862–9880

Pamato M, Novella D, Jacob D, Oliveira B, Pearson D, Greene S, Afonso J, Favero M, Stachel T, Alvaro M, Nestola F (2021) Protogenetic sulfide inclusions in diamonds date the diamond formation event using Re-Os isotopes. Geology 49(8):941–945. https://doi.org/10.1130/G48651.1

Pearson DG, Shirey SB, Harris JW, Carlson RW (1998) Sulphide inclusions in diamonds from the koffiefontein kimberlite, S. Africa: constraints on diamond ages and mantle Re–Os systematics. Earth Planet Sci Lett 160(3–4):311–326

Pearson DG, Brenker FE, Nestola F, McNeill J, Nasdala L, Hutchison MT, Matveev S, Mather K, Silversmit G, Schmitz S et al (2014) Hydrous mantle transition zone indicated by ringwoodite included within diamond. Nature 507(7491):221–224

Piermarini G, Block S (1975) Ultrahigh pressure diamond-anvil cell and several semiconductor phase transition pressures in relation to the fixed point pressure scale. Rev Sci Instrum 46(8):973–979

Raghavan V (2004) Fe–Ni–S (iron-nickel-sulfur). J Phase Equilib Diffus 25(4):373

Rohrbach A, Schmidt MW (2011) Redox freezing and melting in the earth/'s deep mantle resulting from carbon-iron redox coupling. Nature 472(7342):209–212. https://doi.org/10.1038/nature09899

Ryzhenko B, Kennedy GC et al (1973) The effect of pressure on the eutectic in the system Fe–Fes. Am J Sci 273(9):803–810

Saxena S, Eriksson G (2015) Thermodynamics of Fe-S at ultra-high pressure. Calphad 51:202–205. https://doi.org/10.1016/j.calphad.2015.09.009

Sclater JG, Jaupart C, Galson D (1980) The heat flow through oceanic and continental crust and the heat loss of the earth. Rev Geophys 18(1):269. https://doi.org/10.1029/RG018i001p00269

Sharp WE (1969) Melting curves of sphalerite, galena, and pyrrhotite and the decomposition curve of pyrite between 30 and 65 kilobars. J Geophys Res 74(6):1645–1652

Shirey S, Smit K, Pearson D, Walter M, Aulbach S, Brenker F, Bureau H, Burnham A, Cartigny P, Chacko T et al (2019) Diamonds and the mantle geodynamics of carbon. Deep carbon past to present. Cambridge University Press, Cambridge, pp 89–128

Smart K, Tappe S, Simonetti A, Simonetti S, Woodland A, Harris C (2017) Tectonic significance and redox state of paleoproterozoic eclogite and pyroxenite components in the slave cratonic mantle lithosphere, voyageur kimberlite, Arctic Canada. Chem Geol 455:98–119

Stachel T, Harris JW (2008) The origin of cratonic diamonds-constraints from mineral inclusions. Ore Geol Rev 34(1–2):5–32

Stagno V (2019) Carbon, carbides, carbonates and carbonatitic melts in the earth's interior. J Geol Soc 176(2):375–387

Stixrude L, Lithgow-Bertelloni C (2005) Thermodynamics of mantle minerals I. Physical properties. Geophys J Int 162(2):610–632

Stixrude L, Lithgow-Bertelloni C (2011) Thermodynamics of mantle minerals-II. Phase equilibria. Geophys J Int 184(3):1180–1213. https://doi.org/10.1111/j.1365-246X.2010.04890.x

Tange Y, Takahashi E, Ki Funakoshi (2011) In situ observation of pressure-induced electrical resistance changes in zirconium: pressure calibration points for the large volume press at 8 and 35 gpa. High Press Res 31(3):413–418

Terasaki H, Frost DJ, Rubie DC, Langenhorst F (2005) The effect of oxygen and sulphur on the dihedral angle between Fe–O–S melt and silicate minerals at high pressure: implications for Martian core formation. Earth Planet Sci Lett 232(3–4):379–392

Thomson AR, Kohn SC, Bulanova GP, Smith CB, Araujo D, Walter MJ (2014) Origin of sub-lithospheric diamonds from the juina-5 kimberlite (Brazil): constraints from carbon isotopes and inclusion compositions. Contrib Mineral Petrol 168(6):1–29

Tsuno K, Dasgupta R (2015) Fe–Ni–Cu–C–S phase relations at high pressures and temperatures: the role of sulfur in carbon storage and diamond stability at mid-to deep-upper mantle. Earth Planet Sci Lett 412:132–142

Urakawa S, Kato M, Kumazawa M (1987) Experimental study on the phase relations in the system Fe–Ni–O–S up to 15 gpa. High-Press Res Miner Phys 39:95–111

Urakawa S, Someya K, Terasaki H, Katsura T, Yokoshi S, Ki Funakoshi, Utsumi W, Katayama Y, Yi Sueda, Irifune T (2004) Phase relationships and equations of state for Fes at high pressures and temperatures and implications for the internal structure of mars. Phys Earth Planet Inter 143:469–479

Waldner P, Pelton AD (2004) Thermodynamic modeling of the Ni–S system. Int J Mater Res 95(8):672–681

Waldner P, Pelton AD (2005) Thermodynamic modeling of the Fe–S system. J Phase Equilib Diffus 26(1):23–38

Walter MJ, Bulanova GP, Armstrong LS, Keshav S, Blundy JD, Gudfinnsson G, Lord OT, Lennie AR, Clark SM, Smith CB, Gobbo L (2008) Primary carbonatite melt from deeply subducted oceanic crust. Nature 454(7204):622–625. https://doi.org/10.1038/nature07132

Westerlund K, Shirey S, Richardson S, Carlson R, Gurney J, Harris J (2006) A subduction wedge origin for paleoarchean peridotitic diamonds and harzburgites from the panda kimberlite, slave craton: evidence from Re–Os isotope systematics. Contrib Mineral Petrol 152(3):275–294

Zhang Z, Hirschmann MM (2016) Experimental constraints on mantle sulfide melting up to 8 gpa. Am Miner 101(1):181–192

Zhang Z, Lentsch N, Hirschmann MM (2015) Carbon-saturated monosulfide melting in the shallow mantle: solubility and effect on solidus. Contrib Mineral Petrol 170(5):1–13

Zhang Z, von der Handt A, Hirschmann MM (2018) An experimental study of Fe–Ni exchange between sulfide melt and olivine at upper mantle conditions: implications for mantle sulfide compositions and phase equilibria. Contrib Mineral Petrol 173(3):1–18